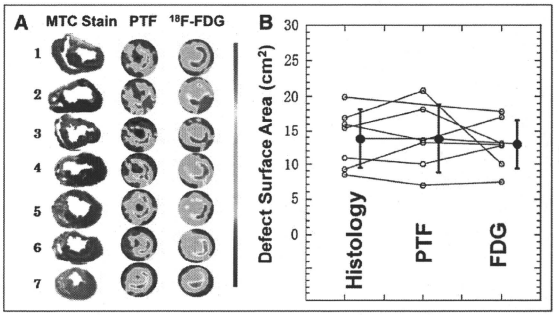

RGB

FIGURE 5. (A) Histologic, PTF, and ^{18}F-FDG slices at middle level of left ventricle in 7 animals of group B. Spatial distribution and size of MI are visually reproducible among animals. Myocardial hypertrophy was visible in remote myocardial wall regions. (B) Comparison of defect surface areas obtained from histologic stained slices with PET images using ^{18}F-FDG and PTF. MTC = Masson trichrome.

knowledge, been accomplished in any studies of pig heart disease. The size of MI reached approximately 27% of the whole left ventricle, causing the remodeling and global LV dilatation (significantly increased LV end-systolic and end-diastolic volumes) to be associated with reduced global LV function. PET with $C^{15}O$ and ^{18}F-FDG showed that regional LV wall motion was impaired not only in the infarcted region but also in the myocardial areas remote from the MI. PET also demonstrated reduced MBF reactivity in remote regions in addition to the infarct area. PTI was also reduced in the remote region, suggesting development of microscopic fibrosis. Moreover, other findings from histology indicated the existence of abnormalities in the noninfarcted area remote from the MI. These results indicate that this animal model may be close to human CHF after MI.

Shen et al. (*16*) adopted additional pacing tachycardia in pigs after sequential coronary artery ligations and observed global LV dysfunction, claiming that CHF was introduced. The present study is similar to the study by Shen et al. (*16*) but is based on only sequential coronary artery obstructions accomplished with acute distal coronary artery occlusion followed by a chronic proximal coronary occlusion with an ameroid constrictor, causing similar LV dysfunction. Of note was the better survival rate (80% at 1 mo, 75% at 4 mo) demonstrated in the current report than in any previous report (*6,8–12,14,16*), including Shen et al.

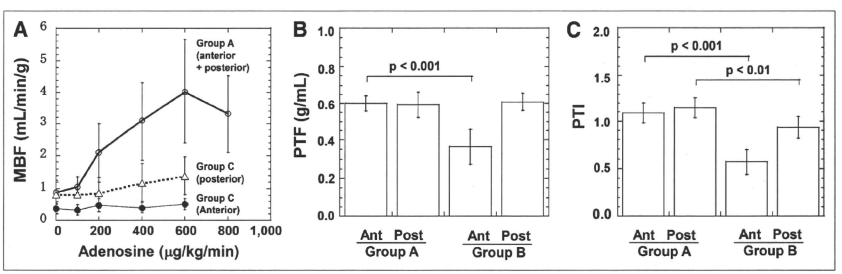

FIGURE 6. Results from PET studies. (A) Regional MBF as function of adenosine dose. In group A, MBF increases with increasing adenosine dose. In infarcted anterior wall of group B, MBF is reduced at rest and does not respond to adenosine. In posterior wall region, adenosine reactivity was significantly reduced. (B and C) Comparison of water-PTF (B) and water-PTI (C). Both were reduced in anterior wall of group B. PTI was also reduced in posterior wall in group B. Ant = anterior; Post = posterior.

jnm084848-pm 36 ■ 4/15/11

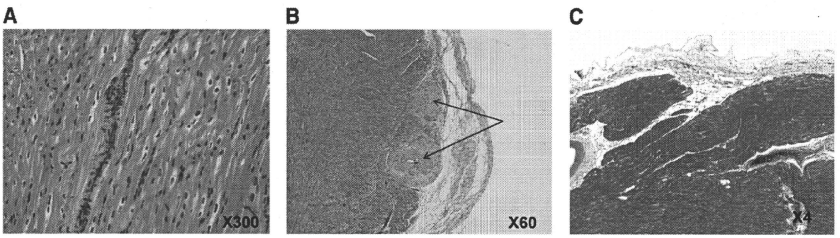

FIGURE 7. Typical images of histologic staining obtained from group B. Hypertrophy with multinuclear muscle cell breeding (A), hyperplasia of blood vessels shown as arrows (B), and denaturation necrosis often seen in subendocardial regions, as in this picture (C), are typical findings.

(73.3% at 21 d). In addition, it has not been confirmed whether such a good survival rate at 21 d could last more than 4 mo after producing global LV dysfunction with MI. Our preliminary experiment, independently performed on 69 farm pigs, demonstrated that when the proximal LAD was occluded by the ameroid constrictor alone, 45 pigs (65%) died within a month, and the total survival rate was 30% at 4 mo. This survival rate is significantly smaller than the rates from the present study.

The reason why animals with MI acquired such good survival is not fully understood. However, it was clearly observed that the ligation of the peripheral coronary artery before the gradual occlusion of the main trunk of the LAD apparently inhibited the fibrillation during the operation. This procedure is obviously effective at protecting against fatal arrhythmias. This preconditioning effect is supported by the experiments of Moses et al. (*27*), in which ischemic preconditioning of the distal coronary artery protected cardiac muscle through a mechanism involving the potassium channels of mitochondria and myocytes. There may be contributions from other preconditioning factors (*9,28–30*) that associate with increased tolerance of ischemia. Another mechanism could be associated with the modulation of sympathetic tone. It has been reported that regional heterogeneity in myocardial cellular mechanisms (responsible for myocardial cellular depolarization) and repolarization in hibernating myocardium (*12*) can induce ventricular fibrillation (*9*). Inhibition of such heterogeneous myocardial cellular mechanisms or control of modulated sympathetic tone could be another possible explanation.

The present study used a gradual total occlusion of the proximal of LAD, as evidenced by the coronary angiography (Fig. 4), and thus caused an MI of approximately 27% of the total myocardium. The global LV ejection fraction in group B was significantly reduced (39% vs. 66% in controls), showing that LV systolic function was impaired in group B. Both histology and PET had concordant findings. The baseline MBF in the MI area was reduced and was not responding to adenosine administration. This finding is reasonable because the infarcted tissue should have reduced capillary density, and the resistive vessels do not respond to any vasodilating stimulation. The physical extent and size of the MI were reproducible among the individual animals. This feature is important when this animal model is applied to evaluate various new pharmaceuticals or various regenerative therapeutic trials.

The noninfarcted myocardium developed clear signs of remodeling, such as hypokinesis, hypertrophy, and the accumulation of fibrotic tissue in the remote myocardial wall, and significantly decreased PTI values, a marker of residual fractionation of water-perfusable tissue. The baseline MBF was preserved, but reactivity to the adenosine was blunted, even at a maximum dose of 600 μg/kg/min. This reduced reactivity could be related to the degeneration of small arteries, possibly caused by enlargement of myocytes and development of moderate denaturation necrosis and fibrosis.

This study demonstrated that physiologic status and physical extent of MI can be evaluated using the noninvasive technique of PET. The defect surface area identified with ^{18}F-FDG was identical to that identified with PTF, and both agreed well with the results of histology. Furthermore, microscopic degeneration can be characterized as reduced reactivity of quantitative myocardial perfusion to adenosine. The PET-derived PTI, which is known to indicate the absolute fraction of non–scar tissue within the area (*22*), was reduced not only in the infarcted anterior wall but also in the remote region by 10%. As demonstrated in recent studies (*31–34*), the reduced PTI in a control region is thought to be caused by the development of microscopic fibrosis.

In this study, left-atrial and LV pressure analyses have not been measured, because the aims of this study were to create a long-survival pig model of MI and global LV dysfunction with remodeling, characterize this model using PET, and compare these parameters with histology before making a complete model of CHF after MI in pigs. One limitation of this study was that, because of technical reasons in our laboratory at the initiation of this study, it was difficult to measure left-atrial and LV pressures.

jnm084848-pm 37 ■ 4/15/11

CONCLUSION

Our pig model of postinfarction global LV dysfunction was characterized by a high survival rate and large MI, with clear signs of cardiac remodeling, as demonstrated by PET and histology. This animal model might contribute to investigations of MI and new therapies for cardiac remodeling in MI.

ACKNOWLEDGMENTS

We thank the staff of the Department of Investigative Radiology of National Cardiovascular Center for invaluable technical assistance. This study was supported by a research grant from New Energy and Industrial Technology Development Organization (NEDO), Japan, and grants for translational research and nanomedicine from the Ministry of Health, Labor and Welfare (MHLW), Japan.

REFERENCES

1. Saito I, Folsom AR, Aono H, Ozawa H, Ikebe T, Yamashita T. Comparison of fatal coronary heart disease occurrence based on population surveys in Japan and the USA. *Int J Epidemiol.* 2000;29:837–844.
2. Balady GJ, Jette D, Scheer J, Downing J. Changes in exercise capacity following cardiac rehabilitation in patients stratified according to age and gender: results of the Massachusetts Association of Cardiovascular and Pulmonary Rehabilitation Multicenter Database. *J Cardiopulm Rehabil.* 1996;16:38–46.
3. Krum H, Haas SJ, Eichhorn E, et al. Prognostic benefit of beta-blockers in patients not receiving ACE-inhibitors. *Eur Heart J.* 2005;26:2154–2158.
4. Anversa P, Leri A, Kajstura J. Cardiac regeneration. *J Am Coll Cardiol.* 2006;47:1769–1776.
5. Gheeraert PJ, Henriques JP, De Buyzere ML, De Pauw M, Taeymans Y, Zijlstra F. Preinfarction angina protects against out-of-hospital ventricular fibrillation in patients with acute occlusion of the left coronary artery. *J Am Coll Cardiol.* 2001;38:1369–1374.
6. Millard RW. Induction of functional coronary collaterals in the swine heart. *Basic Res Cardiol.* 1981;76:468–473.
7. Roth DM, Maruoka Y, Rogers J, White FC, Longhurst JC, Bloor CM. Development of coronary collateral circulation in left circumflex Ameroid-occluded swine myocardium. *Am J Physiol.* 1987;253:H1279–H1288.
8. Fallavollita JA, Riegel BJ, Suzuki G, Valeti U, Canty JM Jr. Mechanism of sudden cardiac death in pigs with viable chronically dysfunctional myocardium and ischemic cardiomyopathy. *Am J Physiol Heart Circ Physiol.* 2005;289:H2688–H2696.
9. Canty JM Jr, Suzuki G, Banas MD, Verheyen F, Borgers M, Fallavollita JA. Hibernating myocardium: chronically adapted to ischemia but vulnerable to sudden death. *Circ Res.* 2004;94:1142–1149.
10. Fallavollita JA, Canty JM Jr. Differential ^{18}F-2-deoxyglucose uptake in viable dysfunctional myocardium with normal resting perfusion: evidence for chronic stunning in pigs. *Circulation.* 1999;99:2798–2805.
11. Fallavollita JA, Canty JM Jr. Ischemic cardiomyopathy in pigs with two-vessel occlusion and viable, chronically dysfunctional myocardium. *Am J Physiol Heart Circ Physiol.* 2002;282:H1370–H1379.
12. Fallavollita JA, Logue M, Canty JM Jr. Stability of hibernating myocardium in pigs with a chronic left anterior descending coronary artery stenosis: absence of progressive fibrosis in the setting of stable reductions in flow, function and coronary flow reserve. *J Am Coll Cardiol.* 2001;37:1989–1995.
13. Shen YT, Vatner SF. Mechanism of impaired myocardial function during progressive coronary stenosis in conscious pigs: hibernation versus stunning? *Circ Res.* 1995;76:479–488.
14. Mills I, Fallon JT, Wrenn D, et al. Adaptive responses of coronary circulation and myocardium to chronic reduction in perfusion pressure and flow. *Am J Physiol.* 1994;266:H447–H457.
15. Roth DM, White FC, Nichols ML, Dobbs SL, Longhurst JC, Bloor CM. Effect of long-term exercise on regional myocardial function and coronary collateral development after gradual coronary artery occlusion in pigs. *Circulation.* 1990;82:1778–1789.
16. Shen YT, Lynch JJ, Shannon RP, Wiedmann RT. A novel heart failure model induced by sequential coronary artery occlusions and tachycardiac stress in awake pigs. *Am J Physiol.* 1999;277:H388–H398.
17. *Guide for the Care and Use of Laboratory Animals.* Washington, DC: National Academy Press; 1996.
18. O'Konski MS, White FC, Longhurst J, Roth D, Bloor CM. Ameroid constriction of the proximal left circumflex coronary artery in swine: a model of limited coronary collateral circulation. *Am J Cardiovasc Pathol.* 1987;1:69–77.
19. Iida H, Takahashi A, Tamura Y, Ono Y, Lammertsma AA. Myocardial blood flow: comparison of oxygen-15-water bolus injection, slow infusion and oxygen-15-carbon dioxide slow inhalation. *J Nucl Med.* 1995;36:78–85.
20. DeFronzo RA, Tobin JD, Andres R. Glucose clamp technique: a method for quantifying insulin secretion and resistance. *Am J Physiol.* 1979;237:E214–E223.
21. Knuuti MJ, Nuutila P, Ruotsalainen U, et al. Euglycemic hyperinsulinemic clamp and oral glucose load in stimulating myocardial glucose utilization during positron emission tomography. *J Nucl Med.* 1992;33:1255–1262.
22. Iida H, Tamura Y, Kitamura K, Bloomfield PM, Eberl S, Ono Y. Histochemical correlates of ^{15}O-water-perfusable tissue fraction in experimental canine studies of old myocardial infarction. *J Nucl Med.* 2000;41:1737–1745.
23. Iida H, Rhodes CG, de Silva R, et al. Myocardial tissue fraction: correction for partial volume effects and measure of tissue viability. *J Nucl Med.* 1991;32:2169–2175.
24. Iida H, Rhodes CG, de Silva R, et al. Use of the left ventricular time-activity curve as a noninvasive input function in dynamic oxygen-15-water positron emission tomography. *J Nucl Med.* 1992;33:1669–1677.
25. de Silva R, Yamamoto Y, Rhodes CG, et al. Preoperative prediction of the outcome of coronary revascularization using positron emission tomography. *Circulation.* 1992;86:1738–1742.
26. Yamamoto Y, de Silva R, Rhodes CG, et al. A new strategy for the assessment of viable myocardium and regional myocardial blood flow using ^{15}O-water and dynamic positron emission tomography. *Circulation.* 1992;86:167–178.
27. Moses MA, Addison PD, Neligan PC, et al. Inducing late phase of infarct protection in skeletal muscle by remote preconditioning: efficacy and mechanism. *Am J Physiol Regul Integr Comp Physiol.* 2005;289:R1609–R1617.
28. Kitakaze M, Node K, Minamino T, et al. Role of activation of protein kinase C in the infarct size-limiting effect of ischemic preconditioning through activation of ecto-5′-nucleotidase. *Circulation.* 1996;93:781–791.
29. Kharbanda RK, Mortensen UM, White PA, et al. Transient limb ischemia induces remote ischemic preconditioning in vivo. *Circulation.* 2002;106:2881–2883.
30. Chen PS, Chen LS, Cao JM, Sharifi B, Karagueuzian HS, Fishbein MC. Sympathetic nerve sprouting, electrical remodeling and the mechanisms of sudden cardiac death. *Cardiovasc Res.* 2001;50:409–416.
31. Knaapen P, Boellaard R, Gotte MJ, et al. Perfusable tissue index as a potential marker of fibrosis in patients with idiopathic dilated cardiomyopathy. *J Nucl Med.* 2004;45:1299–1304.
32. Knaapen P, Boellaard R, Gotte MJ, et al. The perfusable tissue index: a marker of myocardial viability. *J Nucl Cardiol.* 2003;10:684–691.
33. Knaapen P, Bondarenko O, Beek AM, et al. Impact of scar on water-perfusable tissue index in chronic ischemic heart disease: evaluation with PET and contrast-enhanced MRI. *Mol Imaging Biol.* 2006;8:245–251.
34. Knaapen P, van Dockum WG, Bondarenko O, et al. Delayed contrast enhancement and perfusable tissue index in hypertrophic cardiomyopathy: comparison between cardiac MRI and PET. *J Nucl Med.* 2005;46:923–929.

38
jnm084848-pm ■ 4/15/11

Vital Microscopic Analysis of Polymeric Micelle Extravasation from Tumor Vessels: Macromolecular Delivery According to Tumor Vascular Growth Stage

KATSUYOSHI HORI,[1] MASAMICHI NISHIHARA,[2] MASAYUKI YOKOYAMA[2]

[1]Division of Cancer Control, Department of Vascular Biology, Institute of Development, Aging and Cancer, Tohoku University, 4-1 Seiryomachi, Aoba-ku, Sendai, 980-0785 Miyagi, Japan

[2]Kanagawa Academy of Science and Technology, 3-2-1 Sakado, Takatsu-ku, Kawasaki, 213-0012 Kanagawa, Japan

Received 2 March 2009; revised 27 April 2009; accepted 15 May 2009

Published online 18 June 2009 in Wiley InterScience (www.interscience.wiley.com). DOI 10.1002/jps.21848

ABSTRACT: Particles larger than a specific size have been thought to extravasate from tumor vessels but not from normal vessels. Therefore, various nanoparticles incorporating anticancer drugs have been developed to realize selective drug delivery to solid tumors. However, it is not yet clear whether nanoparticles extravasate readily from all tumor vessels including vessels of microtumors. To answer this question, we synthesized new polymeric micelles labeled with fluorescein isothiocyanate (FITC) and injected them into the tail vein of rats with implanted skinfold transparent chambers. We also analyzed, by means of time-lapse vital microscopy with image analysis, extravasation of FITC micelles from tumor vessels at different stages of growth of Yoshida ascites sarcoma LY80. Polymeric micelles readily leaked from vessels at the interface between normal and tumor tissues and those at the interface between tumor tissues and necrotic areas. The micelles showed negligible extravasation, however, from the vascular network of microtumors less than 1 mm in diameter and did not accumulate in the microtumor. Our results suggest that we must develop a novel therapeutic strategy that can deliver sufficient nanomedicine to microtumors. © 2009 Wiley-Liss, Inc. and the American Pharmacists Association J Pharm Sci 99:549–562, 2010

Keywords: cancer; drug targeting; macromolecular drug delivery; micelle; polymeric drug carrier; tumor vessels; permeability; EPR effect; vital microscopy; cancer chemotherapy

INTRODUCTION

Current research on drug delivery systems for solid tumors attaches importance to the concept that nanomedicine technologies, such as encapsulation of anticancer drugs into liposomes or polymeric micelles and polymerization of anticancer drugs, selectively deliver anticancer drugs to tumor tissues by passive targeting.[1–8] This therapeutic strategy is based on the tumor microenvironment and on the following morphological and functional characteristics of tumor vasculature: (i) various kinds of tumors commonly secrete vascular endothelial growth factor/vascular permeability factor (VEGF/VPF),[9–11] (ii) tumor vessels usually have wider intercellular junctions than do normal vessels,[12] (iii) many tumor vessels have fenestrated structures,[13] and (iv) endothelial cells of tumor vessels have more vesiculo-vacuolar organelles than do those of normal vessels.[14]

Intravital microscopic observation has shown, however, that tumor vessels are heterogeneous and that vessels with different morphological characteristics coexist in the same tumor.[15,16] More than 30 years ago, Yamaura and Sato,[15] using a rat transparent chamber, observed the process of tumor growth from initiation to necrosis

Correspondence to: Katsuyoshi Hori (Telephone: +81-22-717-8532; Fax: +81-22-717-8533; E-mail: k-hori@idac.tohoku.ac.jp)

Journal of Pharmaceutical Sciences, Vol. 99, 549–562 (2010)

and classified it into four characteristic stages. They showed that tumor vascular morphology markedly changed according to tumor growth. By using similar tumor cell lines, our previous work demonstrated that microcirculatory functions, such as tumor blood flow (TBF) and tumor interstitial fluid pressure, also markedly changed according to tumor growth.[17,18]

Here, the question of whether nanoparticles leak from all tumor vessels was investigated. This issue is of interest because if nanoparticles do not extravasate from certain tumor vessels, nanomedicines would not reach tissues supplied by such vessels. In such cases, different drug delivery measures would be required. Although this potential problem is a key point in diagnosis and therapy with nanomedicines, many studies of drug delivery systems published to date have not addressed it.

To examine this question, polymeric micelles labeled with fluorescein isothiocyanate (FITC) were synthesized and injected i.v. into rats with implanted transparent chambers. Polymeric micelles have been studied as a carrier system of mainly hydrophobic anticancer drugs.[19,20] Polymeric micelles are self-assembling nanostructures (diameter range, 10–100 nm) that are typically composed of amphiphilic block copolymers. To date, doxorubicin,[21] taxans,[22,23] a derivative of oxaliplatin,[24] camptothecin,[25] a derivative of camptothecin,[26] and an MRI contrast agent[27] have been encapsulated in polymeric micelles, some of which are now in clinical trials.[6]

The specific purposes of the present study were to identify blood vessels from which polymeric micelles readily extravasated and to clarify characteristics of tumor tissues in which such extravasation occurred. A combination of time-lapse vital microscopy and image analysis was used to analyze differences in extravasation of FITC micelles from tumor vessels at different stages of tumor growth. This analysis permitted discussion of the microcirculatory mechanism of accumulation of polymeric micelles or other nanomedicines in tumor tissues.

MATERIALS AND METHODS

Rats and Tumors

Male Donryu rats (Crj-Donryu; Nippon Charles-River, Yokohama, Japan), 7–8 weeks old and with an average weight of 220–250 g, were used for all experiments. Rats were bred and maintained in accordance with The Law (No. 105) and Notification (No. 6) issued by the Japanese Government. Specifically, they were comfortably maintained in a ventilated, temperature-controlled (24 ± 1°C), specific pathogen-free environment on a bed of wood shavings, with food and water freely available and a 12-h light–dark cycle. Rats that were equipped with transparent chambers for vital microscopic observations (see below) were caged singly (cage volume, 30 cm × 40 cm × 25 cm).

A variant of Yoshida sarcoma, LY80, was used in all experiments. This cell line, which can grow in ascites and in solid form, was maintained by successive i.p. transplantation.

All experimental protocols were reviewed by the Committee on the Ethics of Animal Experiments of Tohoku University and were carried out according to the Guidelines for Animal Experiments issued by Tohoku University.

FITC-Labeled Tracers

As a tracer for extravasation of macromolecules into tissues, a new FITC-labeled polymeric micelle was synthesized. First, poly(ethylene glycol)-*b*-poly(β-benzyl-L-aspartate) [PEG_{12}-*b*-$PBLA_{14}$, molecular weight (M_w), 14,900; PEG_{12}, M_w of PEG chain, 12,000; number of BLA units, 14.0] was prepared. PEG_{12}-*b*-$PBLA_{14}$ [500 mg (33.6 μmol)] was dissolved in 3.5 mL of anhydrous dimethyl sulfoxide, and FITC [15.9 mg (40.8 μmol)] (Sigma–Aldrich Japan Co., Tokyo, Japan) was added to the solution.

To confirm the introduction of FITC into PEG_{12}-*b*-$PBLA_{14}$ and the purity of PEG_{12}-*b*-$PBLA_{14}$-FITC, ^{1}H-NMR spectroscopy with a Varian Unity Inova (400 MHz) spectrometer was used with reversed-phase high-performance liquid chromatography. The binding percentage of the terminal portion of the block copolymer with FITC was 67.7%. In principle, FITC is localized at the hydrophobic micellar inner core. Therefore, highly concentrated FITC would be expected to quench fluorescence. To avoid such intramicellar quenching, the optimal molar ratio of PEG_{12}-*b*-$PBLA_{14}$-FITC in micelles was investigated.

The diameter of the FITC micelles was measured by the use of dynamic light scattering. The preliminary experiment confirmed that these micelles had a monophasic half-life *in vivo*.

Another lot of FITC micelles, synthesized by chance in the present study, had a chemical

composition and physical properties that were almost the same [PEG_{12}-*b*-$PBLA_{14}$, M_w, 14,800; M_w of PEG chain, 12,000; number of BLA units, 13.9] as those of the first micelle preparation, but the preparation's half-life was biphasic. It is not yet clear why these two micelle preparations had different *in vivo* behaviors despite having similar structures. A possible reason for this difference is the slight change in the micelle preparation procedure (concentration and scale of preparation). The second micelle system was used only to determine whether the image analysis used had sufficient accuracy to detect two compartments and whether fluorescence intensity measured by the image analysis was quantifiable.

Fluorescein sodium (M_w, 376.3) (Tokyo Chemical Industry Co., Tokyo, Japan) served as the low-molecular-weight tracer. The chemical structure of fluorescein sodium is very similar to that of FITC (M_w, 389.4).

FITC micelles and fluorescein sodium were administered i.v. at doses of 20 and 1 mg/kg, respectively.

Anesthesia

Both pentobarbital sodium salt (Tokyo Kasei Kogyo Co., Tokyo, Japan) and enflurane (Abbott Laboratories, North Chicago, IL) were used for anesthesia. Enflurane is suitable for long experiments in rodents because of its minor irritation of the rat airway, although it cannot be purchased today because newer anesthetics have replaced it. We were able to use enflurane because we had purchased enough in 2007 before a production halt and stocked it at our laboratory. Pentobarbital powder was dissolved in distilled water (Otsuka Pharmaceutical Co., Ltd, Tokyo, Japan) to give a concentration of 50 mg/mL. The solution was administered i.m., 10 min before the experiment, at a dose of 30 mg/kg, and supplemental doses (15 mg/kg i.m.) were given at 90-min intervals to maintain immobilization. Enflurane concentration was maintained at 1% in the inhaled gas, which was administered at a rate of 1 L/min by means of an anesthetic apparatus for small laboratory animals. Hydration of the animals was maintained during anesthesia by i.m. administration of about 0.1 mL of water every 90 min. We confirmed in a previous experiment that our anesthesia conditions caused little disturbance of the microcirculation.

Implantation of Transparent Chambers and Tumor Transplantation

For direct observation of changes in tumor vessels and measurement of extravasation of FITC-labeled compounds, transparent chambers were implanted, under aseptic conditions, in dorsal skin flaps of rats. Transparent chambers used here were a "sandwich" system,[28] with each chamber consisting of a pair of identical titanium frames containing a circular quartz glass window, 10 mm in diameter and 300 μm thick. In this sandwich system, tumor tissue and normal tissue did not overlap. Therefore, extravasation of FITC-labeled compounds into tumor tissue could be analyzed without interference by normal tissue and vice versa. The implantation method was previously described in detail.[29] For tumor transplantation, a small fragment (approximately 0.1 mm^3) of solid tumor from a donor rat was transplanted onto the normal tissue in a transparent chamber while the chamber was being implanted in the dorsal skin flap.

Classification of Growth Stage of the Tumor and Its Vascular System

The tumor and its vascular system growing in the transparent chamber were divided into four stages according to the classification of Yamaura and Sato.[15] The first stage is the beginning of tumor growth. In this stage, tumor cells freely invade surrounding tissue, and many capillaries begin to proliferate and form rapidly growing granulation tissue. The second stage involves exponential tumor growth. In this stage, to support growth, new tumor vascular networks with active and abundant blood flow form. In the third stage, tumor vascular density reaches a plateau, and the tumor growth rate begins to gradually decrease. In this stage, many so-called giant capillaries,[16] which have extremely thin walls and large lumens, appear. The fourth stage is the period of a rapid decrease in tumor vascular density, and tumor tissue degradation progresses. Tumor vessels in this stage run adjacent to necrotic areas, so tumor cord structure[30] is seen. The first- and second-stage tumor vessels and the third- and fourth-stage tumor vessels were monitored 7–9 and 11–14 days after tumor transplantation, respectively.

In the present study, a necrotic area was defined as a tumor region in a transparent chamber in which circulation completely stopped for more

than 24 h and thus the color of the tissue changed to gray. That such a region was a necrotic area was histologically confirmed (Fig. 1).

Vital Microscopic Observation

After anesthesia, each rat with a transparent chamber was placed in the right lateral position on a heated (34.5°C) stage (MATS-SFA; Tokai HIT Co., Tokyo, Japan), which was attached to the mechanical stage of the microscope. Tumor microcirculation in the chamber was transilluminated by a 12-V 100-W halogen lamp and was directly observed with a light microscope (Eclipse E800; Nikon Co., Tokyo, Japan), with a 10× ocular (CFI UW; Nikon Co.) and 2–20× objectives (CFI Plan Fluor; Nikon Co.). Microscopic images were recorded by using a closed-circuit video system consisting of a CCD video camera (CS-900; Olympus Co., Tokyo, Japan), TV monitor (PVM-14M4J; Sony Co., Tokyo, Japan), and S-VHS video recorder (SVO-2100; Sony Co.).

Fluorescence Microscopic Analysis of FITC-Labeled Compounds

Figure 2 provides a schematic illustration of the experimental set-up for fluorescence microscopic analysis of FITC-labeled compounds. For intravital fluorescence microscopy, the light source was changed to a high-pressure mercury lamp (C-SHG1; Nikon Co.). Tumor vessels in the chamber were epi-illuminated and photographed through a 420- to 490-nm primary filter, 505-nm dichroic interference mirror, and 520-nm secondary filter. FITC-labeled compounds were injected into rats as a single i.v. bolus. Microscopic images of extravasation of FITC-labeled compounds were photographed with a silicon-intensified video camera (C2400-08; Hamamatsu Photonics, Hamamatsu, Japan) at 15 time points during the experimental period and were recorded with a video recorder. The maximum ultraviolet (UV) ray exposure time of tissues in transparent chambers at each time point was 6 s. Thus, total exposure time for one rat was less than 90 s. The influence of

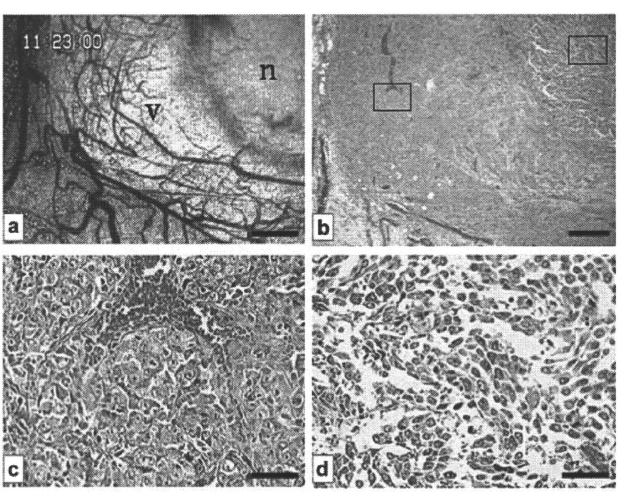

Figure 1. Necrotic area in a tumor observed within a transparent chamber. (a) Vital microscopy. n, necrotic tissue; v, viable tumor tissue. (b) Histology (hematoxylin and eosin). (a) and (b) are the same area. (c) High-power magnification of the left square area in (b). (d) High-power magnification of the right square area in (b). Scale bars represent 250 μm in (a) and (b), and 50 μm in (c) and (d). Histology clearly shows that the gray region [upper right in (a)] with stopped circulation is a necrotic area.

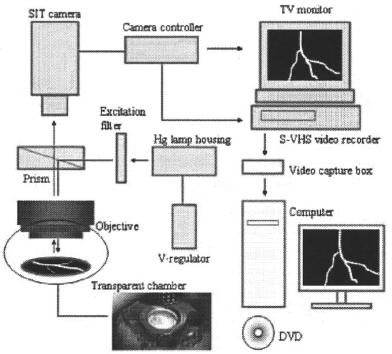

Figure 2. Schematic representation of the vital fluorescence microscopy system. SIT, silicon-intensified target.

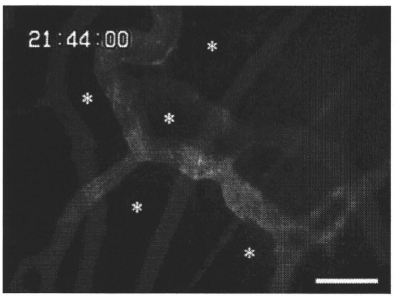

Figure 3. Photograph of extravascular spaces used for measurement of fluorescence intensity, at 4 min after i.v. administration of FITC micelles. Asterisks indicate candidate areas for measurement. Scale bar represents 50 μm.

UV exposure on *in vivo* fluorescence intensity could be ignored because an *in vitro* test without blood circulation showed that the attenuation of fluorescence intensity was less than 10%, even after continuous UV irradiation for 10 min (data not shown). The slight positional change of the observation area that occurred during the long experiment was adjusted every 3–4 h. For precise analysis of the correlation between time after administration of FITC-labeled compounds and fluorescence intensity, a video timer was superimposed on images. Analog images on videotape were converted to digital images by means of a video capture device (PC-MDVD/U2; Buffalo, Inc., Nagoya, Japan). The digital images were recorded on a DVD.

For image analysis, segments of time-lapse images were transferred from the DVD to a computer hard disk (Dimension 9150; Dell Japan, Inc., Kawasaki, Japan). Temporal changes in fluorescence intensity of regions of interest (ROIs) in tissue in the chambers were measured by using NIH Image J (free software). The labeled fluorescent substances circulated in blood vessels only just after i.v. administration (Fig. 3). Therefore, blood vessels and extravascular spaces could easily be distinguished. In the present study, fluorescence intensity in tissues was measured by carefully removing blood vessel areas from the images of the entire tumor tissue. Thus, selected ROIs were distant from the blood vessels. One ROI (10 μm^2) consisted of 100 pixels, and 5–10 ROIs per chamber were randomly selected for analysis.

The parameter $T_{C_{max}}$, which is the time to reach maximum intensity, was defined for evaluation of extravasation of fluorescein sodium. Washout of FITC-labeled compounds from tissues or blood was evaluated by using the half-life ($t_{1/2}$) of fluorescence intensity.[31]

Measurement of Half-Life of FITC Micelles in Blood

To confirm the quantifiability of FITC-micelle half-life evaluated by fluorescence image analysis, the FITC concentration was measured in samples of rat plasma. FITC micelles with the biphasic half-life were used for this experiment. A permanent cannulation method served for blood collection.[32] An arterial cannula was placed in the thoracic aorta of each rat through the left common carotid artery 1 day before injection of FITC micelles. Samples (0.2 mL) of rat blood were obtained from the cannula at multiple time points (i.e., 10 min and 1, 2, 3, 4, 6, and 8 h) after i.v. injection of the FITC-micelle solutions. To minimize the influence of blood collection, blood sampling was limited to twice for each rat. Before blood samples were collected, the inside of the syringe and needle were washed with heparin to prevent blood clotting. Rat plasma samples were obtained by centrifugation (3000 rpm × 5 min). FITC concentrations in plasma samples were determined by using fluorescence spectroscopy (FP-6500 spectrofluorometer; JASCO Co., Tokyo, Japan). The excitation wavelength was set at 495 nm.

Measurement of TBF and Mean Arterial Blood Pressure (MABP)

To ascertain whether polymeric micelles have any effect on circulation, the effect of micelles on TBF and MABP was determined. TBF was measured by using the hydrogen clearance method, as follows. In brief, inhalation of 9% hydrogen gas in air (at 1 L/min) caused tissues to be saturated with hydrogen, after which blood flow (mL/min/100 g tissue) was calculated from the half-life of the clearance curve obtained. This method was previously described in detail.[33] MABP was measured via a catheter inserted into the right femoral artery. Pressure in the catheter was recorded continuously with a pressure transducer (TNF-R; Spectramed Medical Products, Yishun, Singapore), whose output was fed into an amplifier (6M82; NEC-Sanei Co., Tokyo, Japan). TBF and MABP were measured simultaneously at multiple time points (i.e., 1, 5, 10, and 30 min, 1 h, and every hour thereafter until 6 h) after i.v. micelle administration. In this experiment, polymeric micelles formed with PEG_{12}-*b*-$PBLA_{14}$ block copolymer were used.

Statistics

All results are expressed as means ± SD. The statistical significance of the difference between tumor and normal tissues for extravasation of FITC-labeled compounds was evaluated via repeated-measures ANOVA. The *p*-values of 0.05 or lower were considered to be significant.

RESULTS

FITC-Micelle Preparation

Figure 4A shows the chemical structure of the PEG_{12}-*b*-$PBLA_{14}$-FITC block copolymer. The binding percentage of the terminal portion of the block copolymer with FITC was 67.7%. When PEG_{12}-*b*-$PBLA_{14}$-FITC and unlabeled PEG_{12}-*b*-$PBLA_{14}$ were mixed at a ratio of 1:3, that is, when 16.9% (67.7% × 0.25 = 16.9%) of block copolymer constituting the micelles was labeled by FITC, the FITC-micelle preparation did not show self-quenching (data not shown).

The diameter of the FITC micelles was 48.2 ± 8.8 nm (the weight-average diameter ± SD). These micelles were accompanied by a very small amount (<2% by weight) of secondary

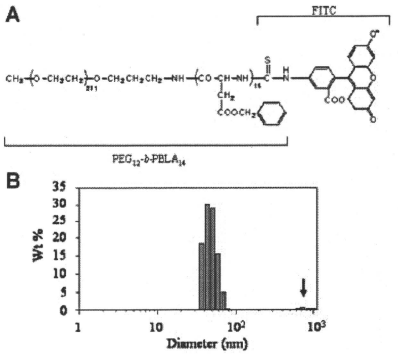

Figure 4. Chemical structure of the PEG_{12}-*b*-$PBLA_{14}$-FITC block copolymer (A), and a weight-average diameter of the dispersed micelles as measured by dynamic light scattering (B). Arrow indicates secondary aggregates.

aggregates with diameters of 208 and 760 nm (Fig. 4B). The basic structure of this micelle system was almost the same as that of the micelle system encapsulating doxorubicin, which was described previously.[21]

Effects of a Polymeric Micelle Preparation on TBF and MABP

Figure 5 shows time changes in TBF and MABP after i.v. administration (40 mg/kg) of a polymeric micelle preparation incorporating PEG_{12}-*b*-$PBLA_{14}$ block copolymer. TBF and MABP did not change significantly during the experimental period of 6 h. A small number of experiments confirmed that the polymer micelles had no influence on MABP and blood flow even at 12 h after administration (data not shown).

Quantifiability of Fluorescence Intensity of FITC Micelles, as Measured by Image Analysis

Figure 6A plots the fluorescence intensity of FITC micelles in an arteriolar vessel as measured by image analysis. Figure 6B shows the FITC concentration in rat plasma samples as measured by fluorescence spectroscopy. Half-life values were calculated from each plot. Both methods produced biphasic washout curves. The half-lives

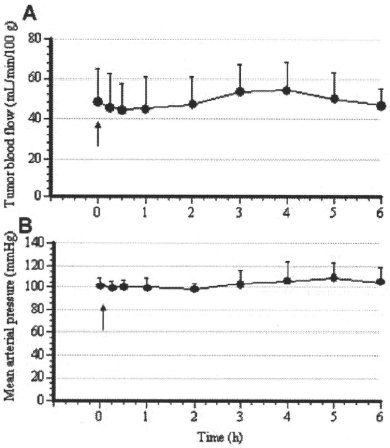

Figure 5. Changes in TBF (A; $n = 15$) and MABP (B; $n = 8$) in rats that received a micelle preparation (40 mg/kg i.v.) incorporating PEG_{12}-*b*-$PBLA_{14}$ block copolymer. The micelle solution was administered at 0 h (arrows). No significant changes were observed during the 6-h experimental period.

of fluorescence intensity in the α- and β-phase were 1.0 and 6.5 h, respectively. The half-lives of FITC concentration in the α- and β-phase were 1.0 and 7.1 h, respectively. The half-life values measured via these two different methods thus corresponded to a considerable degree. This finding indicates that a linear correlation occurred between fluorescence intensity as measured by image analysis and blood concentration of micelles. It was therefore decided that the fluorescence intensity of FITC measured by image analysis could be used as an indicator of micelle concentration.

Extravasation of FITC Micelles from the Vessels in Normal Tissue and Advanced Tumor Tissue

Figure 7A and B presents typical vital microscopic differences in extravasation of FITC micelles between normal tissue and advanced tumor tissue. Figure 7C shows time changes in mean fluorescence intensity of FITC micelles in normal subcutaneous tissues (20 areas from four transparent chambers) and advanced tumor tissues (22 areas from four transparent chambers). Almost no leakage of FITC micelles from normal blood vessels was observed, so the fluorescence intensity of normal tissues was only slightly increased compared with the background value (intensity before FITC-micelle administration) during 12 h of observation. In contrast, FITC micelles began to leak promptly from advanced tumor vessels (mainly the latter half of third-stage vessels), and fluorescence intensity reached a plateau in about 1 h. Washout of FITC micelles from tumor tissue was very slow, however. The difference in

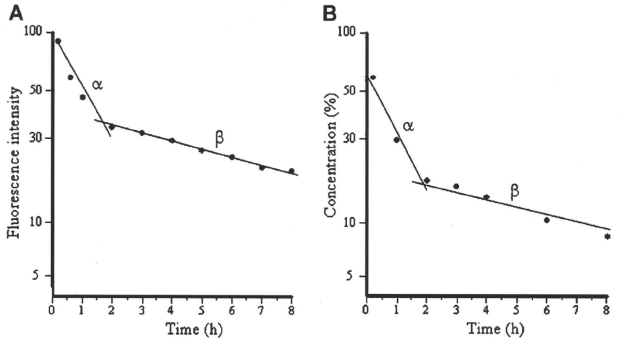

Figure 6. Half-life of FITC micelles in blood as measured by image analysis (A) and spectroscopy (B). Polymeric micelles with a biphasic half-life were used. Half-life values of the α- and β-phase measured by the two different methods showed considerable agreement.

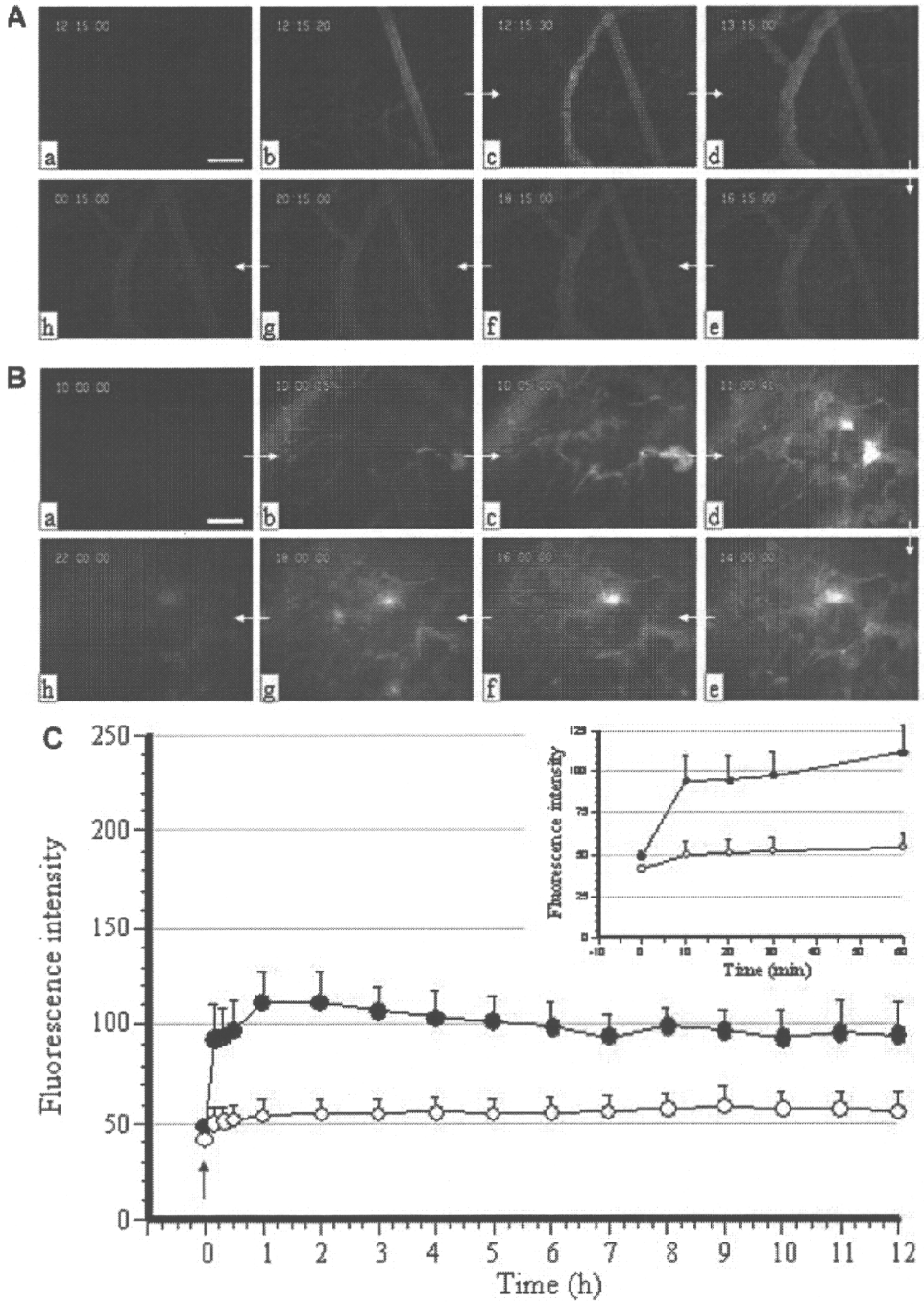

Figure 7. Extravasation of FITC micelles from vessels in normal subcutaneous tissue and advanced tumor tissue. (A) Typical extravasation of FITC micelles from normal tissue. (a) At the start of i.v. FITC micelle (20 mg/kg) administration; (b, c, d, e, f, g, h) 20 s, 30 s, 1 h, 4 h, 6 h, 8 h, and 12 h later, respectively. (B) Typical extravasation of FITC micelles from advanced tumor tissue. (a) At the beginning of FITC-micelle (20 mg/kg) administration; (b, c, d, e, f, g, h) 15 s, 5 min, 1 h, 4 h, 6 h, 8 h, and 12 h later, respectively. Arrows indicate the direction of time; scale bars represent 100 μm. (C) Time changes in fluorescence intensity of FITC micelles in normal tissue (○) ($n = 20$) and advanced tumor tissue (●) ($n = 22$). Small graph indicates the changes in 0–1 h. The micelle solution was administered i.v. at 0 h (arrow). Maximum fluorescence intensity was 255. Extravasation of FITC micelles was markedly high in the advanced tumor.

DOI 10.1002/jps

fluorescence intensity of FITC micelles in normal tissues and advanced tumor tissues was highly significant ($p < 0.001$).

Figure 8 presents typical vital microscopic changes in extravasation and washout of fluorescein sodium, used as a positive control, after i.v. administration. Fluorescein sodium was evenly and promptly distributed to all tissues, that is, nontumor tissue, tumor tissue, and the interface between nontumor and tumor tissues. Fluorescence intensity reached a maximum at about 3 min ($T_{C_{max}}$, 2.5–3 min) after i.v. administration, and fluorescein sodium was completely washed out from all tissues 150 min later ($t_{1/2}$, 45–55 min). No marked differences in $T_{C_{max}}$ and $t_{1/2}$ occurred among the three different areas.

Extravasation and Retention of FITC Micelles in Tumor Tissue, Including Necrotic Areas

Figure 9A presents typical extravasation of FITC micelles in tumor tissue, including necrotic areas. Figure 9B shows time changes in fluorescence intensity in tissues during the 16 h after i.v. administration of FITC micelles. FITC micelles readily extravasated from fourth-stage tumor vessels near a necrotic area. These FITC micelles first diffused into viable tumor tissue, which received blood from the vessels, and then gradually infiltrated nearby necrotic tissues where they accumulated. Although a concentration gradient occurred between necrotic and viable tissues until several hours after administration of FITC micelles, both tissues showed almost equal FITC-micelle concentrations 9 h later, which indicated that micelles moved from viable tumor tissues to necrotic tissues.

Extravasation and Retention of FITC Micelles in and Around Microtumors

Figure 10A presents typical extravasation of FITC micelles in and around a microtumor, less than 1 mm in diameter. Figure 10B shows the time course of fluorescence intensity in tumor tissue during 24 h after i.v. administration of micelles. Vascular networks in this microtumor were all composed of second-stage tumor vessels, which had an active, high flow rate. Extravasation of micelles from the second-stage tumor vessels was very low and was approximately the same as that from normal vessels. Also, FITC micelles did not accumulate in tumor tissues of this stage. Extravasation of micelles from the vessels of the interface between normal tissue and tumor tissue was very high. In such a microtumor, however, FITC micelles that had extravasated into the interface did not remain there (Fig. 10Aj).

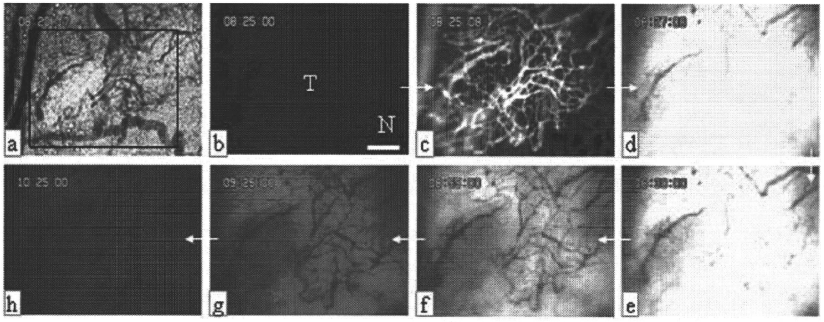

Figure 8. Extravasation of fluorescein sodium from vessels in normal and tumor tissues and washout from those tissues. Fluorescein sodium (1 mg/kg) was administered i.v. (a) Vital microscopy. The black frame is the observation area. (b) At the start of micelle administration; (c) 8 s later; (d) 2 min later; (e) 5 min later; (f) 30 min later; (g) 1 h later; (h) 2 h later. T, tumor; N, normal tissue. Arrows indicate the direction of time; scale bar represents 200 μm. No marked differences in extravasation and washout between normal and tumor tissues were found.

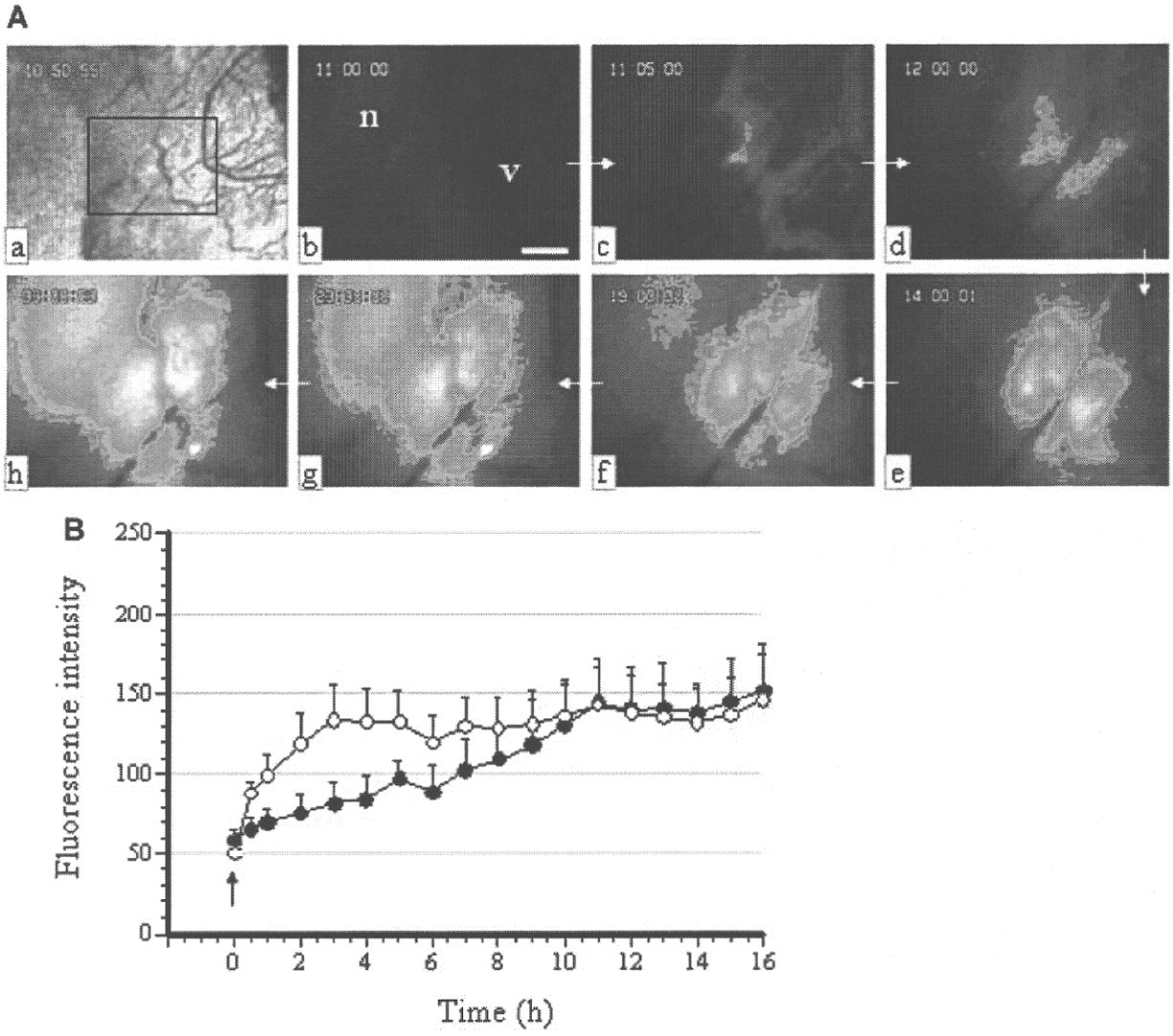

Figure 9. Extravasation and retention of FITC micelles in tumor tissue, including necrotic areas. The FITC-micelle preparation (20 mg/kg) was administered i.v. (A) Typical extravasation of FITC micelles in tumor tissue including necrotic areas. (a) Vital microscopy. The black frame is the observation area. (b) At the start of micelle administration; (c) 5 min later; (d) 1 h later; (e) 3 h later; (f) 8 h later; (g) 12 h later; (h) 16 h later. n, Necrotic tissue; v, viable tumor tissue. Arrows indicate the direction of time; scale bar represents 100 μm. (B) Time changes in fluorescence intensity of FITC micelles in viable tumor tissue (○) ($n = 5$) and necrotic tumor tissue (●) ($n = 5$). The micelle solution was administered i.v. at 0 h (arrow). Maximum fluorescence intensity was 255. Note that micelles moved from viable tumor tissues to necrotic tissues and stayed there.

DISCUSSION

The present study used an FITC-labeled tracer to investigate the *in vivo* behavior of polymeric micelles. To analyze the *in vivo* behavior of such macromolecules with a long half-life in blood, it is important to perform prolonged monitoring. Although some studies have shown extravasation of fluorescent macromolecules by means of intravital fluorescence microscopy,[34–36] the monitoring time in many cases was 2 h or less. In our study reported here, determination of optimal anesthesia conditions permitted lengthy *in vivo* observations, so that marked variations in extravasation and intratumor retention of these micelles according to tumor growth stage could be demonstrated.

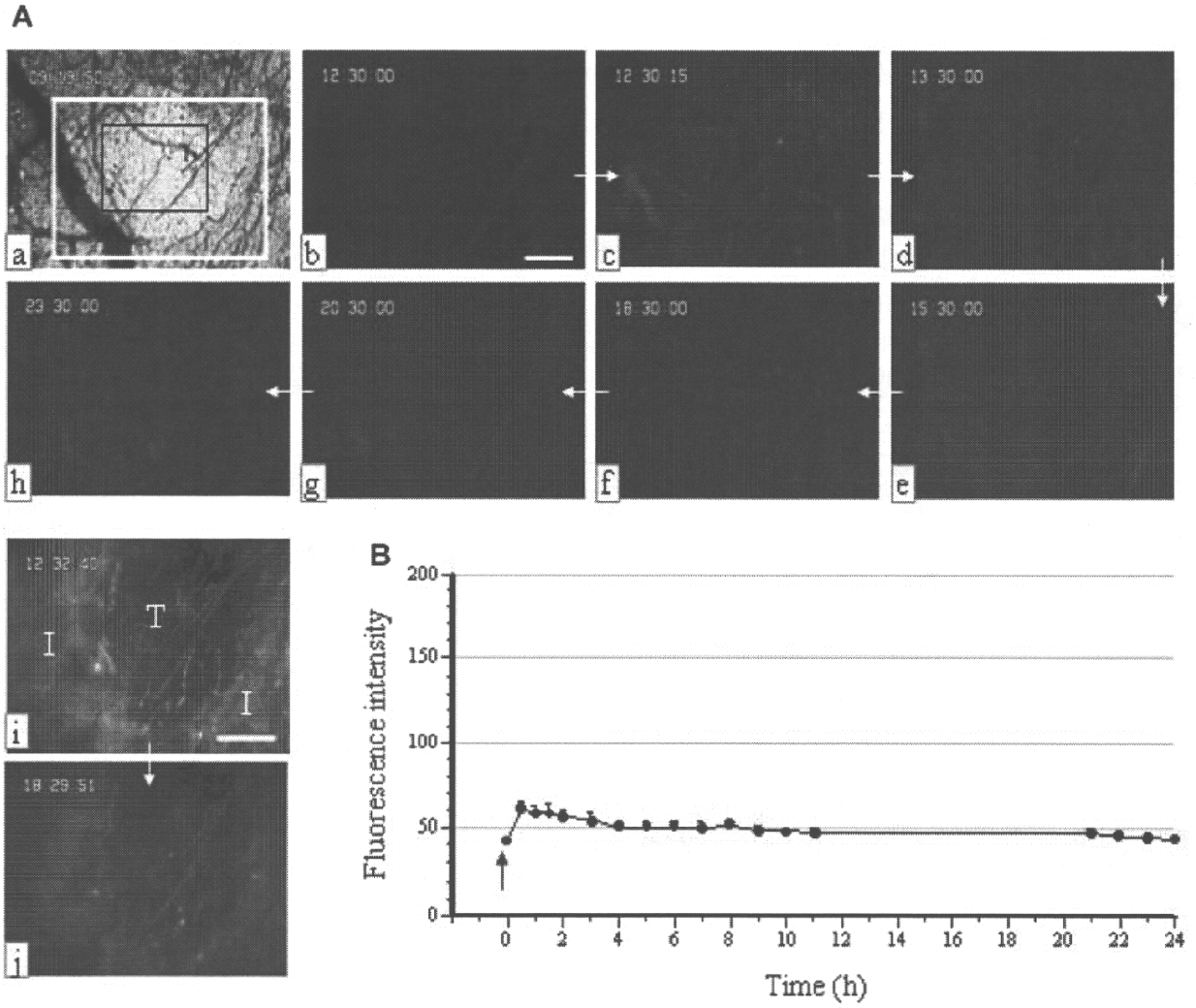

Figure 10. Behavior of FITC micelles in and around microscopic tumor foci. The FITC-micelle solution (20 mg/kg) was administered i.v. (A) Vital microscopy. (a) The black frame is the observation area of (b)–(h) and the white frame is the area of (i) and (j). (b) At the start of micelle administration; (c) 15 s later; (d) 1 h later; (e) 3 h later; (f) 6 h later; (g) 8 h later; (h) 11 h later. (i) 160 s later (low magnification). T, microscopic tumor; I, interface between normal tissue and tumor tissue. (j) 6 h later (low magnification). Arrows indicate the direction of time; scale bars represent 100 and 300 μm in (b) and (i), respectively. (B) Time changes in fluorescence intensity of FITC micelles in tumor tissue ($n = 8$). The micelle solution was administered i.v. at 0 h (arrow). Maximum fluorescence intensity was 255. Note that extravasation of FITC micelles was negligible in the microscopic tumor.

The half-life calculated by means of image analysis agreed well with that determined by fluorescence spectroscopy. Blood flow stabilization is essential for the calculation of the half-life of substances in a tissue. If tissue blood flow changes in an irregular fashion, individual time points plotted for the half-life would not lie in a logarithmic line. Although some macromolecules disturb tumor microcirculation and change TBF in such a way (data not shown), polymeric micelles used in the present study did not directly influence TBF and MABP. It was therefore concluded that fluorescence intensity measured by our image analysis method accurately reflected micelle concentration.

With regard to extravasation of low-molecular-weight compounds from vessels, normal tissue and tumor tissue exhibited no marked differences.

Fluorescein sodium showed almost equal extravasation into normal tissue and tumor tissue and almost equal washout from those tissues. However, although leakage of polymeric micelles from normal vessels was slight, it occurred readily from vessels at the interface between normal tissue and tumor tissue (i.e., the area consisting of granulation tissue caused by cancer cells infiltrating normal tissues) and from tumor vessels at the interface between tumor tissue and necrotic areas.

Yamaura and Matsuzawa[37] examined the permeability of tumor vessels to Brilliant Blue 6B (Pontamine sky blue), which is an albumin-binding dye. They reported almost no increase in permeability in second-stage vessels and the first half of third-stage vessels, whereas permeability to the dye was greatly increased in first-stage vessels and was abnormally high in fourth-stage vessels in and around necrotic tumor tissue. Our present results agreed with their observations, because almost all vessels at the interface between normal and tumor tissues were first-stage vessels, and many vessels at the interface between tumor tissue and necrotic areas corresponded to fourth-stage tumor vessels.

Advanced tumors usually include areas of necrosis. In such tumors, polymeric micelles extravasated from tumor vessels (mainly fourth-stage vessels) that were adjacent to these necrotic areas gradually infiltrated necrotic areas and remained there for a long time. This phenomenon is clearly the enhanced permeability and retention (EPR) effect described by Maeda and Matsumura.[2–6] It is believed that the main driving force of this gradual movement of micelles is circulatory movement of interstitial fluid, because an interstitial fluid flow rate of 2–3 mL/min/100 g was detected even in tumor tissue in which TBF was completely stopped (Hori et al., unpublished work).

Polymeric micelle accumulation in necrotic tumor areas is believed to result in part from weak intratumor drainage, as Maeda et al.[2] emphasized. Although it has been thought that tumors do not have lymph vessels, recent immunohistological studies revealed many lymphatic endothelial cells in tumors.[38] However, evidence strongly suggests that the drainage function of the lymphatic system is quite weak.[39,40] Intratumor lymphatic endothelial cells may construct functionally incomplete lymph vessels. Clearance of polymeric micelles once delivered to the tissue would thereby be markedly suppressed. Another of our experiments showed that when circulation was functional, as in an irradiated tumor, polymeric micelles did not accumulate in necrotic tumor areas (data not shown). This observation also supports Maeda's concept. In view of the result that FITC concentration in necrotic tissue rose above that in blood more than 10 h after i.v. administration of FITC micelles, micelles may be absorbed by such tissues. This question warrants further investigation. However, regardless of the reasons, abundant polymeric micelles clearly accumulate in necrotic tumor tissue with impaired circulatory function.

If anticancer drug-incorporating nanoparticles in necrotic tumor tissue continue to slowly release the anticancer drug, viable cancer cells near this tissue would be exposed to the drug for a long time. Enhanced cancer therapeutic efficacy of nanomedicines, which has been reported,[4,6] may be a function, in part, of this mechanism.

In contrast to an advanced tumor, a microscopic tumor less than 2–3 mm in diameter had no necrotic area, and the circulatory function of its microvascular network was extremely active. The present study found almost no accumulation of polymeric micelles in such microtumors. The primary reason was the extremely low extravasation of micelles from vessels in microscopic tumors (i.e., second-stage tumor vessels) compared with that from vessels in advanced tumors. In fact, almost no difference in extravasation of polymeric micelles from vessels was seen between second-stage tumor vessels and normal blood vessels. A similar tendency was also found for FITC albumin (data not shown).

Various kinds of tumor cells secrete VEGF/VPE.[9–11] Therefore, VEGF tends to be regarded as the most important permeability factor in tumors. However, in view of the present results—that polymeric micelles readily extravasated from first-stage tumor vessels, which are affected by inflammation, and from fourth-stage tumor vessels, which are undergoing degradation—not only VEGF/VPF but also classical inflammation-related permeability factors such as histamine, serotonin, bradykinin, and prostaglandin E_2 may play a relatively important role in extravasation of polymeric micelles.

Taken together, our findings suggest that microscopic metastatic foci may escape from the attack of nanomedicines that encapsulate an anticancer drug.

In conclusion, polymeric micelles can be selectively delivered to tumor tissues. However, to

enhance the therapeutic effect of cancer chemotherapy with the use of nanomedicines, including anticancer drug-incorporating micelles, a means that can deliver sufficient nanomedicine to microtumors and ensure its presence there for a long period must be developed. Such a novel therapeutic strategy against microtumors will be described in a separate article.

ACKNOWLEDGMENTS

We thank Dr. H. Yamaura for his valuable comments about the classification of tumor vessels and Ms. H. Oikawa for expert technical assistance. This work was supported by grants H18-nano-004 for Scientific Research from the Ministry of Health, Labor and Welfare, Japan, and 19591449 for Scientific Research from the Ministry of Education, Science, Sports and Culture, Japan (K.H.), by JST, CREST, and by the Program for Promoting the Establishment of Strategic Research Centers, Special Coordination Funds for Promoting Science and Technology, the Ministry of Education, Culture, Sports, Science, and Technology, Japan (M.N. and M.Y.).

REFERENCES

1. Matsumura Y, Maeda H. 1986. A new concept for macromolecular therapeutics in cancer chemotherapy: Mechanism of tumoritropic accumulation of proteins and the antitumor agent smancs. Cancer Res 46:6387–6392.
2. Maeda H, Wu J, Sawa T, Matsumura Y, Hori K. 2000. Tumor vascular permeability and EPR effect for macromolecular therapeutics. J Control Release 65:271–284.
3. Ferrari M. 2005. Cancer nanotechnology: Opportunity and challenges. Nat Rev Cancer 5:161–171.
4. Duncan R. 2006. Polymer conjugates as anticancer nanomedicines. Nat Rev Cancer 6:688–701.
5. Greish K. 2007. Enhanced permeability and retention of macromolecular drugs in solid tumors: A royal gate for targeted anticancer nanomedicines. J Drug Target 15:457–464.
6. Matsumura Y. 2008. Poly(amino acid) micelle nanocarriers in preclinical and clinical studies. Adv Drug Deliv Rev 60:899–914.
7. Lammers T, Hennink WE, Storm G. 2008. Tumour-targeted nanomedicines: Principles and practice. Br J Cancer 99:392–397.
8. Campbell RB, Ying BO, Kuesters GM, Hemphill R. 2009. Fighting cancer: From the bench to bedside using second generation cationic liposomal therapeutics. J Pharm Sci 98:411–429.
9. Senger DR, Galli SJ, Dvorak AM, Perruzzi CA, Harvey VS, Dvorak HF. 1983. Tumor cells secrete a vascular permeability factor that promotes accumulation of ascites fluid. Science 219:983–985.
10. Dvorak HF, Sioussat TM, Brown LF, Berse B, Nagy JA, Sotrel A, Manseau EJ, Van de Water L, Senger DR. 1991. Distribution of vascular permeability factor (vascular endothelial growth factor) in tumors: Concentration in tumor blood vessels. J Exp Med 174:1275–1278.
11. Ferrara N, Gerber HP, LeCouter J. 2003. The biology of VEGF and its receptors. Nat Med 9:669–676.
12. Long DM. 1970. Capillary ultrastructure and the blood-brain barrier in human malignant brain tumors. J Neurosurg 32:127–144.
13. Roberts WG, Palade GE. 1997. Neovasculature induced by vascular endothelial growth factor is fenestrated. Cancer Res 57:765–772.
14. Feng D, Nagy JA, Hipp J, Dvorak HF, Dvorak AM. 1996. Vesiculo-vacuolar organelles and the regulation of venule permeability to macromolecules by vascular permeability factor, histamine, and serotonin. J Exp Med 183:1981–1986.
15. Yamaura H, Sato H. 1974. Quantitative studies on the developing vascular system of rat hepatoma. J Natl Cancer Inst 53:1229–1240.
16. Warren BA. 1979. The vascular morphology of tumors. In: Peterson HI, editor. Tumor blood circulation. Boca Raton, FL: CRC Press. pp. 1–47.
17. Hori K, Saito S, Sato Y, Akita H, Kawaguchi T, Sugiyama K, Sato H. 2003. Differential relationship between changes in tumour size and microcirculatory functions induced by therapy with an antivascular drug and with cytotoxic drugs: Implications for the evaluation of therapeutic efficacy of AC7700 (AVE8062). Eur J Cancer 39:1957–1966.
18. Hori K, Suzuki M, Abe I, Saito S. 1986. Increased tumor tissue pressure in association with the growth of rat tumors. Jpn J Cancer Res 77:65–73.
19. Yokoyama M. 2005. Polymeric micelles for the targeting hydrophobic drugs. In: Kwon GS, editor. Drug and pharmaceutical sciences, Vol. 148, Polymeric drug delivery systems. Boca Raton, FL: Taylor & Francis. pp. 533–575.
20. Aliabadi HM, Lavasanifar A. 2006. Polymeric micelles for drug delivery. Expert Opin Drug Deliv 3:139–162.
21. Yokoyama M, Okano T, Sakurai Y, Fukushima S, Okamoto K, Kataoka K. 1999. Selective delivery of adriamycin to a solid tumor using a polymeric micelle carrier system. J Drug Target 7:171–186.
22. Hamaguchi T, Matsumura Y, Suzuki M, Shimizu K, Goda R, Nakamura I, Nakatomi I, Yokoyama M, Kataoka K, Kakizoe T. 2005. NK105, a paclitaxel-incorporating micellar nanoparticle formulation, can extend in vivo antitumor activity and reduce

the neurotoxicity of paclitaxel. Br J Cancer 92:1240–1246.
23. Liu B, Yang M, Li X, Qian X, Shen Z, Ding Y, Yu L. 2008. Enhanced efficiency of thermally targeted taxanes delivery in a human xenograft model of gastric cancer. J Pharm Sci 97:3170–3181.
24. Cabral H, Nishiyama N, Kataoka K. 2007. Optimization of (1,2-diamino-cyclohexane) platinum (II)-loaded polymeric micelles directed to improved tumor targeting and enhanced antitumor activity. J Control Release 121:146–155.
25. Yokoyama M, Opanasopit P, Maitani Y, Kawano K, Okano T. 2004. Polymer design and incorporation method for polymeric micelle carrier system containing water-insoluble anti-cancer agent camptothecin. J Drug Target 12:373–384.
26. Koizumi F, Kitagawa M, Negishi T, Onda T, Matsumoto S, Hamaguchi T, Matsumura Y. 2006. Novel SN-38-incorporating polymeric micelles, NK012, eradicate vascular endothelial growth factor-secreting bulky tumors. Cancer Res 66:10048–10056.
27. Shiraishi K, Kawano K, Minowa T, Maitani Y, Yokoyama M. Preparation and in vivo imaging of PEG-poly(L-lysine)-based polymeric micelle MRI contrast agents. J Control Release (in press).
28. Yamaura H, Suzuki M, Sato H. 1971. Transparent chamber in the rat skin for studies on microcirculation in cancer tissue. Gann 62:177–185.
29. Hori K, Suzuki M, Tanda S, Saito S. 1990. In vivo analysis of tumor vascularization in the rat. Jpn J Cancer Res 81:279–288.
30. Thomlinson RH, Gray LH. 1955. The histological structure of some human lung cancers and the possible implications for radiotherapy. Br J Cancer 9:539–549.
31. Hori K, Furumoto S, Kubota K. 2008. Tumor blood flow interruption after radiotherapy strongly inhibits tumor regrowth. Cancer Sci 99:1485–1491.
32. Popovic V, Popovic P. 1960. Permanent cannulation of aorta and vena cava in rats and ground squirrels. J Appl Physiol 15:727–728.
33. Hori K, Saito S, Nihei Y, Suzuki M, Sato Y. 1999. Antitumor effects due to irreversible stoppage of tumor tissue blood flow: Evaluation of a novel combretastatin A-4 derivative, AC7700. Jpn J Cancer Res 90:1026–1038.
34. Chen B, Pogue BW, Luna JM, Hardman RL, Hoopes PJ, Hasan T. 2006. Tumor vascular permeabilization by vascular-targeting photosensitization: Effects, mechanism, and therapeutic implications. Clin Cancer Res 12:917–923.
35. Dreher MR, Liu W, Michelich CR, Dewhirst MW, Yuan F, Chilkoti A. 2006. Tumor vascular permeability, accumulation, and penetration of macromolecular drug carriers. J Natl Cancer Inst 98:335–344.
36. He C, Agharkar P, Chen B. 2008. Intravital microscopic analysis of vascular perfusion and macromolecule extravasation after photodynamic vascular targeting therapy. Pharm Res 25:1873–1880.
37. Yamaura H, Matsuzawa T. 1979. Tumour regrowth after irradiation. An experimental approach. Int J Radiat Biol 35:201–219.
38. Ji RC. 2006. Lymphatic endothelial cells, tumor lymphangiogenesis and metastasis: New insights into intratumoral and peritumoral lymphatics. Cancer Metastasis Rev 25:677–694.
39. Padera TP, Kadambi A, di Tomaso E, Carreira CM, Brown EB, Boucher Y, Choi NC, Mathisen D, Wain J, Mark EJ, Munn LL, Jain RK. 2002. Lymphatic metastasis in the absence of functional intratumor lymphatics. Science 296:1883–1886.
40. Pathak AP, Artemov D, Ward BD, Jackson DG, Neeman M, Bhujwalla ZM. 2005. Characterizing extravascular fluid transport of macromolecules in the tumor interstitium by magnetic resonance imaging. Cancer Res 65:1425–1432.

Pharmaceutical Research, Vol. 27, No. 2, February 2010 (© 2009)
DOI: 10.1007/s11095-009-0018-9

Research Paper

Accelerated Blood Clearance Was Not Induced for a Gadolinium-Containing PEG-poly(L-lysine)-Based Polymeric Micelle in Mice

Huili Ma,[1] Kouichi Shiraishi,[2] Takuya Minowa,[1] Kumi Kawano,[1] Masayuki Yokoyama,[2,3] Yoshiyuki Hattori,[1] and Yoshie Maitani[1,4]

Received July 6, 2009; accepted November 24, 2009; published online December 25, 2009

Purpose. Accelerated blood clearance (ABC) is induced by repeated injections of PEGylated liposomes. In this study, the ABC was investigated for a gadolinium-containing PEG-poly(L-lysine)-based polymeric micelle (Gd-micelle) and PEGylated liposome (Gd-liposome) in mice.

Materials and Methods. Effects of the first injection of Gd-micelle on the tissue distribution of the second dose of Gd-micelle were studied. Additionally, effects of the first injection of Gd-micelle, Gd-liposome, empty liposome, polyethyleneglycol ($PEG_{500,000}$), and PEG-lipid on the distribution of the second dose of the Gd-liposome were evaluated.

Results. Results indicated that the tissue distribution of the second injection of the Gd-micelle at a dose of 33, 5, or 2 μmol Gd/kg was not affected by the first injection of the Gd-micelle at different doses and time intervals or of the empty PEGylated liposome 7 days before. ABC of Gd-liposome at a dose of 2.3 μmol Gd/kg (corresponding to 10 μmol lipids/kg) was observed when the empty PEGylated liposome or Gd-liposome, but not the Gd-micelle, $PEG_{500,000}$ or PEG-lipid, was pre-administered.

Conclusions. The hydrophobic core of the micelle or lipid bilayer of PEGylated liposome has a major effect on this phenomenon. These studies have significant implications for the evaluation of PEG-poly (L-lysine)-based micellar formulation of Gd-based contrast agents.

KEY WORDS: accelerated blood clearance; gadolinium; PEGylated liposome; polyethylene glycol (PEG); polymeric micelle.

INTRODUCTION

Long-circulating liposomes with surface-modified polyethyleneglycol (PEG) are often used as carriers of therapeutic agents, since they avoid capture by the reticuloendothelial system (RES) and can extend the systemic circulation time of agents, thereby improving drug delivery (1,2). It was hypothesized that PEG on the surface of liposomes forms a water shell, resulting in decreased adsorption of opsonins and subsequent phagocytosis by cells of the RES (3,4). However, PEGylated liposomes are known to lose their long-circulating property with multiple dosing. Recently, it has been reported that the first dose of PEGylated liposomes injected intravenously caused a loss of the long-circulating property and extensive accumulation in the liver at the second dose injected several days later in mice, rats, rabbit, and rhesus monkeys (5–11), a phenomenon known as accelerated blood clearance (ABC). Besides PEGylated liposomes, other nanocarriers, such as nanoparticles containing PEG, also produced this phenomenon (12). Therefore, ABC would have a significant impact on the application of long-circulating liposomes and nanoparticles with multiple administrations. In clinical applications of liposomal carriers, Gabizon *et al.* reported a reduced clearance of doxorubicin-containing PEGylated liposome in the repeated injections. This opposite behavior to the ABC phenomenon resulted from toxic activity of the encapsulated doxorubicin against the RES (13). Presently, the ABC phenomenon is not a problem in a cancer chemotherapy by the use of a PEG-liposomal carrier, whereas the ABC phenomenon in human clinics must be important for less toxic drug or gene delivery applications of the PEGylated liposomes.

To date, studies of ABC have focused mainly on PEGylated liposomes. Many factors can affect the extent to which ABC is induced by PEGylated liposomes. First of all, the dose of lipid plays an important role, with ABC enhanced at lower concentrations of lipid (6,7,12). Second, ABC occurs in a time-dependent manner (5,7). The time interval between the first and second doses is a key factor. Third, when the amount of PEGylated lipid in the first injection was ≤5 mol%, the second dose of PEGylated liposomes was eliminated more quickly from plasma than liposomes containing >10 mol% PEGylated lipid injected as a first dose (7,8). In addition, the ABC phenomenon

[1] Institute of Medicinal Chemistry, Hoshi University, 2-4-41 Ebara, Shinagawa-ku, Tokyo 142-8501, Japan.
[2] Kanagawa Academy of Science and Technology, Yokoyama "Nanomedical Polymer" Project, KSP East 404, Sakado 3-2-1, Takatsu-ku, Kawasaki, Kanagawa 213-0012, Japan.
[3] Medical Engineering Laboratory, Research Center for Medical Science, Jikei University School of Medicine, 3-25-8, Nishi-shinbashi, Minato-ku, Tokyo 105-8461, Japan.
[4] To whom correspondence should be addressed. (e-mail: yoshie@hoshi.ac.jp)

was reported to be independent of liposomal size, surface charge, and PEG molecular weight (5,7,8).

During the past decade, polymeric micelles, supramolecular assemblies of block copolymers, have demonstrated their utility in drug delivery systems and are currently recognized as promising nanocarriers for enhancing the efficacy of drugs and genes (14–16). Since ABC has a considerable impact on the multiple drug administration, it is necessary to study whether the phenomenon is induced by repeated injections of polymeric micelles. Gadolinium (Gd)-based contrast agents are widely used in magnetic resonance imaging (MRI) to improve the conspicuity of lesions or visualization of blood vessels (17). However, these agents are rapidly cleared from the circulation. To overcome this problem, nanocarriers, such as liposomes and polymeric micelles, are used to encapsulate the agents so as to prolong their circulation and allow them to accumulate in tumors for diagnosis (18–20). If polymeric micelles containing a diagnostic agent cause the ABC phenomenon, then circulation time will be reduced after a second dose and the accuracy of the diagnosis will be affected. Furthermore, polymeric micelles containing MRI agents or drugs administered during diagnosis and treatment will lose some of their drug efficacy because of the accelerated clearance. Hence, it is of great importance to know whether the ABC phenomenon can be induced by polymeric micelles or not. Recently, the accelerated clearance of [^{3}H]-labeled PEGylated liposomes was observed in mice pre-administered with an empty polymeric micelle composed of poly (ethylene glycol)-*b*-poly (β-benzyl L-aspartate) (PEG-PBLA) 50 nm in diameter (16).

In this study, we first investigated whether the ABC effect was caused by repeated injections of a polymeric micelle encapsulating Gd-DOTA (Gd-micelle) and of a PEGylated liposome encapsulating Gd-DTPA (Gd-liposome) as a positive control. Concentrations of Gd ions were measured for this investigation. Furthermore, we examined the effect of a PEG homopolymer on the tissue distribution of Gd-liposomes.

MATERIALS AND METHODS

Materials

Magnevist® (Gd-DTPA) was purchased from Bayer Schering Pharma (Berlin, Germany). 1,2-distearoyl-sn-glycero-3-phosphoethanolamine-n-[methoxy(polyethylene glycol)-2000] (mPEG$_{2000}$-DSPE), hydrogenated soy bean phosphatidylcholine (HSPC), and egg phosphatidylcholine (EPC) were purchased from the NOF Corporation (Tokyo, Japan). Cholesterol and polyethylene glycol 500,000 (PEG$_{500,000}$) were of analytical grade (Wako Pure Chemical, Osaka, Japan). All lipids were used without further purification. All other reagents were of analytical grade.

Animals

Four-week-old female ddY mice were purchased from Sankyo Lab Service Corp. (Tokyo, Japan). All care and handling of animals were performed with the approval of the Animal and Ethics Review Committee of Hoshi University and of Principles of Laboratory Animal Care (NIH #publication 85-23, revised in 1985).

Preparation of the Gd-micelle

Synthesis of a chelate moiety-binding block copolymer was performed as reported in our previous paper (19). Briefly, a poly(ethylene glycol)-*b*-poly(L-lysine) block copolymer (PEG-P(Lys)) was prepared through acid hydrolysis of a poly(ethylene glycol)-*b*-poly[ε-(benzyloxycarbonyl)-L-lysine] (PEG-P(Lys(Z)) block copolymer (Fig. 1). We synthesized PEG-P(Lys(Z) with polymerization of a Lys(Z) *N*-carboxy anhydride monomer from PEG-NH$_2$ (molecular weight of PEG-NH$_2$ = 5,200). 1,4,7,10-Tetraazacyclododecane-1,4,7,10-tetraacetic acid mono (*N*-hydroxysuccinimide ester) was fully conjugated to lysine residues of PEG-P(Lys).

The composition of PEG-P(Lys-DOTA) was determined by means of ^{1}H-NMR spectroscopy in D_2O under alkali conditions (pH>10). $GdCl_3 \cdot 6H_2O$ was added to PEG-P(Lys-DOTA) at pH 6.0 to 6.5 for 3 hr at 50°C. Gd content was determined using inductively coupled plasma (ICP) (SPS7800, SII Nano Technology Inc., Tokyo, Japan). We obtained the block copolymer as PEG-P(Lys-DOTA-Gd) (Gd content = 7.7 wt%, the number average of Gd is 8.2). The block copolymer formed a polymeric micelle spontaneously in an aqueous solution (Gd-micelle). The size and zeta-potential of the Gd-micelle diluted with saline for three independent preparations was 84.5±6.0 nm and −1.70±0.80 mV, respectively, at 25°C as determined by dynamic light scattering (ELS-Z2, Otsuka Electronics Co., Ltd., Osaka, Japan).

Preparation of the Empty Liposome and Gd-liposome

First, an empty liposome, which induced the ABC phenomenon, was prepared by the lipid film hydration method as described previously (21). Briefly, a mixture of HSPC, cholesterol, and mPEG$_{2000}$-DSPE in a molar ratio of 1.85:1.0:0.15 was dissolved in chloroform. The solution was

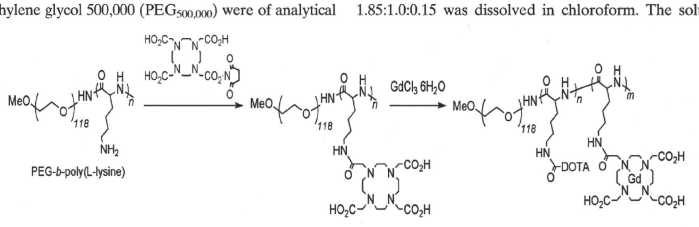

Fig. 1. Synthesis of PEG-P(Lys-DOTA-Gd).

evaporated dry to form the lipid film. Then, the liposome was produced by hydration of the lipid film with saline, followed by size reduction with sonication. The size and zeta-potential of the liposome diluted with saline were 178.5 nm and −22.1 mV, respectively.

Two kinds of Gd-liposomes were prepared because Gd-DTPA content was dependent on the preparation methods. One kind of Gd-liposome was prepared by an ethanol injection method (GdL-E). In brief, a mixture of EPC, cholesterol, and $mPEG_{2000}$-DSPE in a molar ratio of 2.15:0.88:0.15 was dissolved in ethanol and then hydrated with Gd-DTPA at 50°C. The resulting liposomes were sonicated for 10 min, then subjected to exhaustive dialysis against phosphate-buffered saline (PBS, 137 mM NaCl, 8.10 mM Na_2HPO_4, 2.68 mM KCl, 1.47 mM KH_2PO_4, pH 7.4) with a dialysis membrane having a 2,000 molecular-weight cutoff for 24 hr. The size and zeta-potential of the liposome were 150.1±18.8 nm and −0.94±6.78 mV, respectively, for three independent preparations. As a control of GdL-E, an empty liposome not including Gd-DTPA (empty GdL-E) was prepared by the same method as the Gd-liposome (GdL-E), except that saline was used to hydrate the ethanol solution of lipid. The particle size of empty GdL-E was 139.5 nm. Another kind of Gd-liposome was prepared by reverse phase evaporation (GdL-R) to encapsulate a larger amount of Gd-DTPA. The lipid was the same as GdL-E described above and dissolved in 4 mL of chloroform and 2 mL of diethyl ether. Gd-DTPA was added to the lipid solution. The mixture was sonicated to form an emulsion, which was evaporated to produce the liposome. Finally, the resulting liposome was sized at 60°C on an extruder (Avanti Polar Lipids, Inc., AL, USA) with three passes through a 0.4 μm Nuclepore membrane (Waterman, Maidstone, UK) and five passes through a 0.2 μm Nuclepore membrane, followed by exhaustive dialysis as described above. The particle size and zeta-potential of the liposome were 140.9± 13.5 nm and −2.52±5.18 mV, respectively, for three independent preparations. The phospholipid concentration of the liposome including HSPC or EPC was measured with the Phospholipids C-test Wako (Wako Pure Chemical Industries, Ltd.). GdL-E contained 2.26 μmol Gd per 10 μmol lipids, and GdL-R contained 2.29 μmol Gd per 5 μmol lipids.

Release Studies of Gd-micelle and Gd-liposomes

The release of Gd−DTPA from Gd−liposome (GdL−E or GdL−R) and Gd from Gd−micelle was evaluated by dialysis method using a Spectrapor 6 tubing with molecular weight cut-off of 1,000 Da (Spectrum Laboratories Inc., Tokyo, Japan). Briefly, the sample of Gd-micelle containing 1.2 mM Gd and Gd-liposomes of GdL-E containing 0.96 mM Gd-DTPA or GdL-R containing 0.96 mM Gd-DTPA (1 mL) were dialyzed against PBS (pH 7.4, 200 mL) at 37°C. At the indicated time points (10 min, 1, 3, 6, 24 h), 1 mL aliquots of the medium were withdrawn, and the same volume of fresh medium was added. The Gd concentration was analyzed by ICP. The accumulative release of Gd or Gd-DTPA released from the Gd-micelle or Gd-liposome, respectively was expressed as a percentage of the released Gd or Gd-DTPA and plotted as a function of time.

Pharmacokinetics and Tissue Distribution of the Gd-micelle and Gd-liposome

For pharmacokinetics study, the mice were intravenously injected with the Gd-micelle at a dose of 33 μmol Gd/kg (67.3 mg polymer/kg) or the Gd-liposomes including GdL-E at a dose of 6.75 μmol Gd/kg and 10 μmol lipids/kg and GdL-R at 2.65 μmol Gd/kg and 5 μmol lipids/kg. About 30 to 100 μL of blood were taken from a tail vein with a quantitative capillary at 10 min, 1 h, 3 h, 6 h, and 24 h after the injection. The Gd-micelle or the Gd-liposome was injected into a lower part of a tail vein, and blood sample was taken at a certain time point described above from an upper part of the tail vein at the other side of the injected vein. Therefore, this experiment was free from the sample pollution problem. The blood samples were added to saline and centrifuged at 3,000 rpm for 15 min, and the supernatant was used to measure Gd content by ICP. The elimination half-life ($T_{1/2}$) was calculated based on a single compartment model. For the tissue distribution of Gd-micelles and Gd-liposomes study, the second dose of Gd-micelles or Gd-liposomes was injected intravenously through the tail vein at a certain time interval after the first injection. Samples of blood were taken from the hepatic portal vein 6 h after the second injection, and tissues of liver, spleen, and kidney were removed at the same time. The plasma and blood volume were calculated as 0.0488 mL/g body weight for plasma and 0.0778 mL/g body weight for blood, respectively (19).

Measurement of Gd Content

For the quantitative determination of Gd content, blood samples were centrifuged at 3,000 rpm for 15 min, and then plasma was taken out and diluted with 0.1% HNO_3 for ICP. Tissue samples of the liver, spleen, and kidney were digested with a mixture of 98% H_2SO_4 and 62% HNO_3 (1:2, *v:v*) and then subjected to ICP.

Statistical Analysis

The statistical analysis was performed with the Dunnett's multiple comparison test. The level of significance was set at $p<0.05$ or $p<0.01$.

RESULTS

Release Behavior of Gd-micelle and Gd-liposomes

Gd or Gd-DTPA release behavior from Gd-micelle or Gd-liposomes was studied by the dialysis method. As shown in Fig. 2, only 0.2% of Gd leaked from the Gd-micelle at 37°C in PBS (pH 7.4) for 24 h. On the other hand, 4.8% of entrapped Gd-DTPA leaked from the Gd-liposome prepared by reverse phase evaporation method (GdL-R) and 22.4% for 24 h from the Gd-liposome prepared by ethanol injection method (GdL-E). Hence, it is obvious that Gd-micelle has hardly release behavior of Gd, and GdL-R showed much slower release than GdL-E. The results indicated that the leakage of Gd or Gd-DTPA from nanocarriers was greatly affected by the preparation methods.